TOPOLOGICAL MATTER

Chiral Majorana fermion modes in a quantum anomalous Hall insulator–superconductor structure

Qing Lin He,[1]*† Lei Pan,[1]† Alexander L. Stern,[3] Edward C. Burks,[4] Xiaoyu Che,[1] Gen Yin,[1] Jing Wang,[5,6] Biao Lian,[6] Quan Zhou,[6] Eun Sang Choi,[7] Koichi Murata,[1] Xufeng Kou,[1,8]* Zhijie Chen,[4] Tianxiao Nie,[1] Qiming Shao,[1] Yabin Fan,[1] Shou-Cheng Zhang,[6]* Kai Liu,[4] Jing Xia,[3] Kang L. Wang[1,2]*

Majorana fermion is a hypothetical particle that is its own antiparticle. We report transport measurements that suggest the existence of one-dimensional chiral Majorana fermion modes in the hybrid system of a quantum anomalous Hall insulator thin film coupled with a superconductor. As the external magnetic field is swept, half-integer quantized conductance plateaus are observed at the locations of magnetization reversals, giving a distinct signature of the Majorana fermion modes. This transport signature is reproducible over many magnetic field sweeps and appears at different temperatures. This finding may open up an avenue to control Majorana fermions for implementing robust topological quantum computing.

Majorana fermion, proposed by Ettore Majorana in 1937 (*1*), is a putative elementary spin-1/2 particle with the unusual property of being its own antiparticle. In condensed-matter systems, analogs of Majorana fermions can be realized as quasiparticles of topological states of quantum matter, such as the $\nu = 5/2$ quantum Hall state (*2*), Moore-Read–type states in the fractional quantum Hall effect (*3*), two-dimensional (2D) $p_x + ip_y$ spinless superconductors (*4*), strong spin-orbit coupling semiconductor-superconductor heterostructures (*5*, *6*), and ferromagnetic atomic chains on a superconductor (*7*, *8*). Viewed as a superconducting analog of the quantum Hall state (*9*), a chiral topological superconductor (TSC) in two dimensions has a full pairing gap in the bulk and an odd number $\mathcal{N}$ gapless chiral Majorana fermion modes at the edge (*10*, *11*). The fundamental aspects of the Majorana fermion modes and their non-Abelian braiding properties can be potentially used to implement topological qubits in fault-tolerant quantum computation (*12*–*15*). Numerous schemes to accommodate Majorana fermion modes in superconductors coupled with topological matter have been proposed (*16*–*31*). The Majorana zero mode, a 0D version of the Majorana fermion, is a charge-neutral bound state that exists strictly at zero energy. Its existence could be spectroscopically demonstrated by the "zero-bias conductance anomalies" modulated by external electrical/magnetic fields (*20*–*27*, *32*). Although these observations provide promising signatures of Majorana bound states, it is difficult to energetically resolve the contributions from other effects, such as Kondo correlations, Andreev-bound states, weak antilocalization, and reflectionless tunneling (*20*–*22*, *33*–*35*).

In contrast, a recent theoretical proposal focuses on the direct transport signatures of the 1D Majorana fermion modes (*16*–*18*). The 1D Majorana fermion mode satisfies the propagating wave equation originally proposed by Ettore Majorana (*1*). A series of theoretical results (*16*–*18*, *36*) suggests that a chiral TSC based on a quantum anomalous Hall insulator (QAHI) might be a promising host of 1D Majorana fermion modes because the chiral Hall state can be achieved without strong external magnetic fields, preserving superconductivity. To break time-reversal symmetry, the single-domain phase of the QAHI requires an external field of ~0.1 T, which is more than one order of magnitude lower than the critical field of typical superconducting metals. By modulating the external field, topological transitions can lead eventually to the establishment of single chiral Majorana edge modes (CMEMs).

When a superconductor is coupled to a QAHI thin film—i.e., a magnetic topological insulator thin film—a reversal of the magnetization can induce a series of topological phase transitions. The proposed scheme is demonstrated in Fig. 1A, (i) to (vii), where a superconducting region is introduced in the middle of a QAHI channel. The effective Hamiltonian of the QAHI region is written as $\mathcal{H}_0 = \sum_{\mathbf{k}} \psi_{\mathbf{k}}^{\dagger} H_0(\mathbf{k}) \psi_{\mathbf{k}}$, with $\psi_{\mathbf{k}} = (c_{\mathbf{k}\uparrow}^t, c_{\mathbf{k}\downarrow}^t, c_{\mathbf{k}\uparrow}^b, c_{\mathbf{k}\downarrow}^b)^T$ and $H_0(\mathbf{k}) = k_y \sigma_x \tilde{\tau}_z - k_x \sigma_y \tilde{\tau}_z + m(\mathbf{k})\tilde{\tau}_x + \lambda\sigma_z$, where $c_{\mathbf{k}\sigma}$ annihilates an electron of momentum $\mathbf{k}$ and spin $\sigma = \uparrow, \downarrow$; superscripts t and b denote the top and bottom surface states, respectively; σ_i and $\tilde{\tau}_i (i = x, y, z)$ are the Pauli matrices for spins and for the two surfaces, respectively, whereas λ is the exchange field along the z axis induced by the perpendicular ferromagnetic ordering (*18*, *37*). $m(\mathbf{k}) = m_0 + m_1(k_x^2 + k_y^2)$ describes the hybridization between the top and bottom surfaces, which is responsible for opening a trivial surface gap (the Chern number $\mathcal{C} = 0$ state). m_0 and m_1 are the hybridization gap and the parabolic band component, respectively. The Chern number of the system is $\mathcal{C} = \lambda / |\lambda|$ for $|\lambda| > |m_0|$, where $|\mathcal{C}|$ is equal to the number of the chiral edge channels; for $|\lambda| < |m_0|$, $\mathcal{C}$ becomes 0. As a result, by adjusting the external magnetic field, a transition between a normal insulator (NI) with $\mathcal{C} = 0$ (zero plateau, Hall conductance $\sigma_{xy} = 0$) to a QAHI with $\mathcal{C} = \pm 1$ (integer plateau, $\sigma_{xy} = \pm e^2/h$) can be achieved (*38*, *39*). In the middle of the QAHI bar, the proximity to an s-wave superconductor drives the QAHI into a superconducting regime, where a finite superconducting pairing amplitude is induced to the surface of the QAHI, and in this case the system can be described by the Bogoliubov–de Gennes (BdG) Hamiltonian $\mathcal{H}_{\mathrm{BdG}} = \sum_{\mathbf{k}} \Psi_{\mathbf{k}}^{\dagger} H_{\mathrm{BdG}} \Psi_{\mathbf{k}} / 2$, where $\Psi_{\mathbf{k}} = [(c_{\mathbf{k}\uparrow}^t, c_{\mathbf{k}\downarrow}^t, c_{\mathbf{k}\uparrow}^b, c_{\mathbf{k}\downarrow}^b), (c_{-\mathbf{k}\uparrow}^{t\dagger}, c_{-\mathbf{k}\downarrow}^{t\dagger}, c_{-\mathbf{k}\uparrow}^{b\dagger}, c_{-\mathbf{k}\downarrow}^{b\dagger})]^T$, and

$$H_{\mathrm{BdG}} = \begin{pmatrix} H_0(\mathbf{k}) - \mu & \Delta_{\mathbf{k}} \\ \Delta_{\mathbf{k}}^{\dagger} & -H_0^*(-\mathbf{k}) + \mu \end{pmatrix},$$

$$\Delta_{\mathbf{k}} = \begin{pmatrix} i\Delta_1\sigma_y & 0 \\ 0 & i\Delta_2\sigma_y \end{pmatrix}$$

Here, μ is the chemical potential and $\Delta_{1,2}$ are the pairing gap functions of the top and bottom surface states, respectively (*17*, *18*, *36*). In principle, each chiral edge state in the quantum Hall regime is topologically equivalent to two identical copies of CMEMs, such that the total Chern number is even ($\mathcal{N} = 2\mathcal{C}$ in this case). The key to achieving a single CMEM is to induce a topological phase with an odd Chern number to separate the two copies of CMEMs (*16*). When the structural symmetry is preserved between the top and bottom surface states—i.e., $\Delta = \Delta_1 = \Delta_2$—the topological transition in the TSC region can only occur between $\mathcal{N} = \pm 2$ [Fig. 1A, (i) and (vii)] and $\mathcal{N} = 0$ (iv), where the QAHI regions experience a NI-QAHI-NI transition, thanks to the surface hybridization. The topological phase transitions for all three regions are synchronized, and the two CMEMs cannot be distinguished from each other. However, when the structural inversion symmetry is broken, the pairing amplitudes of the top and bottom surfaces are different ($\Delta_1 \neq \Delta_2$), and phases with $\mathcal{N} = \pm 1$ [Fig. 1A, (ii), (iii), (v), and (vi)] emerge (*17*, *18*, *36*). The half-integer conductance of the system can be derived from the scattering matrix for the two QAHI edge states at the entrance and exit of

[1]Department of Electrical and Computer Engineering, Department of Physics, and Department of Materials Science and Engineering, University of California, Los Angeles, CA 90095, USA. [2]King Abdulaziz City for Science and Technology (KACST), Center of Excellence in Green Nanotechnology, Riyadh, Saudi Arabia. [3]Department of Physics and Astronomy, University of California, Irvine, CA 92697, USA. [4]Physics Department, University of California, Davis, CA 95616, USA. [5]State Key Laboratory of Surface Physics, Department of Physics, Fudan University, Shanghai 200433, China. [6]Department of Physics, Stanford University, Stanford, CA 94305, USA. [7]National High Magnetic Field Laboratory, Florida State University, Tallahassee, FL 32310-3706, USA. [8]School of Information Science and Technology, ShanghaiTech University, Shanghai 200031, China.
*Corresponding author. Email: qlhe@ucla.edu (Q.L.H.); kouxf@shanghaitech.edu.cn (X.K.); szhang@stanford.edu (S.-C.Z.); wang@ee.ucla.edu (K.L.W.)
†These authors contributed equally to this work.

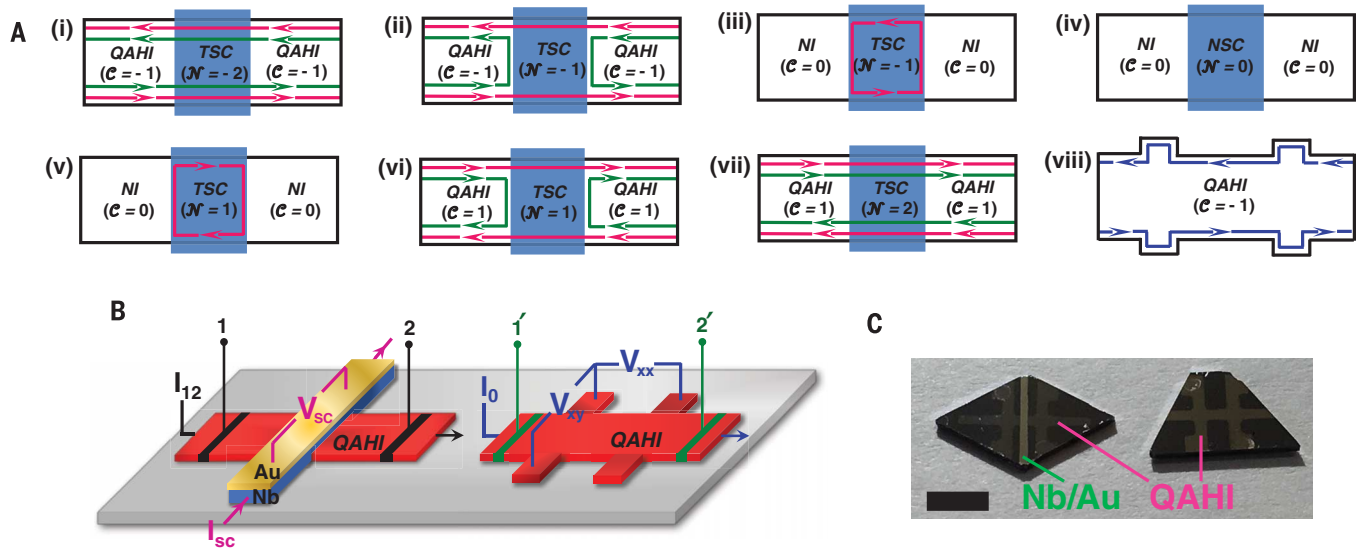

Fig. 1. Chiral Majorana edge modes in the quantum anomalous Hall insulator–superconductor structure. (**A**) The edge transport configurations of the topological superconductor device as shown in the left of (B) evolve during a sweep of the external magnetic field (i) to (vii). This sweep starts by saturating the magnetization along +*z* (i), and then the field is reduced to zero. Further increasing the field along −*z* initiates the reversal of the magnetization (ii). During this reversal, the QAHI enters the trivial insulating state ($\mathcal{C}$ = 0), such that the system evolves to (iii), (iv), and (v), consecutively. When the magnetization is close to a full saturation along −*z*, the transport configuration is driven to (vi). Finally, when a large negative field is applied to fully reverse the magnetization, the system ends up with (vii). Likewise, when the field is swept from −*z* to +*z*, the system evolves in a similar manner, but the current directions are opposite to those in (i) to (vii). Pink and green arrows represent the CMEMs. There is no normal backscattering for $\mathrm{TSC}_{\mathcal{N}=\pm2}$ [(i) and (vii)], while Majorana modes transmit through the $\mathrm{TSC}_{\mathcal{N}=\pm1}$ [(ii) and (vi)]. The last Hall bar (viii) demonstrates the example of the $\mathcal{C}$ = −1 chiral edge transport in a QAHI. (**B**) Schematics of a TSC device consisting of a QAHI $(Cr_{0.12}Bi_{0.26}Sb_{0.62})_2Te_3$ thin film (6 nm thick) and a superconductor Nb bar. A QAHI Hall bar was also fabricated on the same wafer as a reference. The four-terminal longitudinal conductance (σ_{12}) of the TSC device was obtained by passing a current (I_{12}) and measuring the potential drop across points 1 and 2. To characterize the upper critical field ($\mu_0 H_{C2}^{\perp}$) of the Nb bar, its temperature-dependent resistance was measured using an independent four-probe method by passing a current I_{SC} and measuring the voltage V_{SC} under different perpendicular magnetic field strengths (see also Fig. 2A, inset). On the right side, to obtain the Hall conductance (σ_{xy}) of the QAHI device, longitudinal (V_{xx}) and transverse (V_{xy}) voltages were measured when passing a current I_0. The potential drop across the entire Hall bar (V_{12}') was also independently measured to calculate its total longitudinal conductance (σ_{12}'). (**C**) Images of the device structures. (Left) QAHI Hall bar with a Nb/Au bar covering the central part. (Right) Standard QAHI Hall bar. The scale bar is 5 mm in length.

the TSC, which allows for a calculation of the propagation of charge and, therefore, the electrical conductivity (see the supplementary text).

To experimentally identify the CMEM, we fabricate a QAHI-TSC device (Fig. 1B). The QAHI bar with dimensions of 2 mm by 1 mm is implemented using a magnetic topological insulator thin film $(Cr_{0.12}Bi_{0.26}Sb_{0.62})_2Te_3$ grown on a GaAs (111)B substrate by molecular beam epitaxy. The Fermi level is within the surface gap without the assistance of electric-field tuning with a gate (*38*). Because the hybridization gap, m_0, is important to control the proposed topological phase change, the QAHI film thickness is precisely controlled to be six quintuple layers, i.e., around 6 nm (*38*, *40*). Across the central part of the QAHI bar, a superconductor bar (8 mm by 0.6 mm) is deposited, which contains a 200-nm layer of Nb protected by a 5-nm layer of Au. A control QAHI Hall bar of the same dimension is also fabricated near the TSC device on the same wafer. The field-dependent total longitudinal conductance (σ_{12}) is obtained by passing an alternating current (I_{12} in Fig. 1B) through the outer two probes and measuring the potential drop across the inner two probes (Fig. 1B, points 1 and 2). In the control QAHI device, transverse and longitudinal resistivities are obtained using the standard Hall bar setup (Fig. 1B, right).

The single CMEM corresponding to $\mathcal{N}$ = ±1 can be identified experimentally by a unique transport signature of a half-integer longitudinal conductance plateau (0.5 e^2/h) during the reversal of the magnetization (*17*, *18*, *36*). When the external field is large enough, the device fully reaches the QAHI scheme ($\mathcal{C}$ = ±1). In the TSC region, both of the two CMEMs exist, forming the phase of $\mathcal{N}$ = ±2. Because the two CMEMs are topologically equivalent to one QAHI state ($\mathcal{C}$ = ±1), all incident edge modes can almost perfectly transmit through the device, as shown in Fig. 1A, (i) and (vii) [compared with (viii) in the QAHI regime], leading to $\sigma_{12} = e^2/h$ (to be discussed in Fig. 2C). When the magnetic field is reduced, the TSC region experiences the first topological phase change, leading to $\mathcal{N}$ = ±1, such that one of the paired CMEMs vanishes. Because the QAHI regions are still in the $\mathcal{C}$ = ±1 phase, the incident QAHI state can transmit only one of the CMEMs to the TSC region, whereas the other CMEM is almost perfectly reflected. This leads to the separation between the two CMEMs in the incident QAHI state [Fig. 1A, (ii) and (vi)], such that a half-integer plateau of the longitudinal conductance would occur (to be discussed in Fig. 2C). Further reducing the magnetic field drives the QAHI regions to the NI phase ($\mathcal{C}$ = 0), where the surface hybridization gap shuts down the conducting channels (σ_{12} = 0). Although the TSC region still experiences two more topological transitions ($\mathcal{N}$ = −1, 0, 1), no current should go through in these cases, as shown in Figs. 1A, (iii), (iv), and (v). Thus, during every reversal of the magnetization, σ_{12} presents a half-integer plateau close to the coercive fields.

The transport channel formed by the CMEM of $\mathcal{N}$ = ±1 is experimentally demonstrated by the longitudinal conductance signal of the QAHI-TSC device. Figure 2A illustrates the temperature-dependent upper critical field ($\mu_0 H_{C2}^{\perp}$) in the out-of-plane direction of the Nb bar using a standard four-probe method (magenta configuration in Fig. 1B). Here, the zero-resistance temperature (corresponding to the temperature at which the zero-resistance state is just achieved) is extracted from the temperature-dependent resistance characteristics under different perpendicular magnetic fields (Fig. 2A, inset). The resulting $\mu_0 H_{C2}^{\perp}$ shows a linear temperature dependence, which follows the standard linearized Ginzburg-Landau theory for 2D superconductors. For comparison,

the temperature-dependent coercive field ($\mu_0 H_C$) of the QAHI derived from the Hall measurements (fig. S1) is plotted in the same figure. Because $\mu_0 H_{C2}^{\perp}$ is more than one order of magnitude larger than $\mu_0 H_C$ of the QAHI, the superconductivity is ensured even when the QAHI is driven into a single magnetic domain regime under a relatively large external magnetic field. At 350 mK, two longitudinal conductance (σ_{12}) plateaus show up at the low-field shoulders of the σ_{12} valleys in Device I (Fig. 2B). These plateaus occur at ~+80 mT, with conductance values of 0.49 e^2/h. The plateaus at the high-field shoulders cannot be resolved as clearly as the low-field ones. They appear as kinks valued at 0.51(±0.05) e^2/h. The pertinent data obtained from other two TSC devices (II and III) exhibit 0.52(±0.06) and 0.48(±0.07) e^2/h conductance plateaus at a

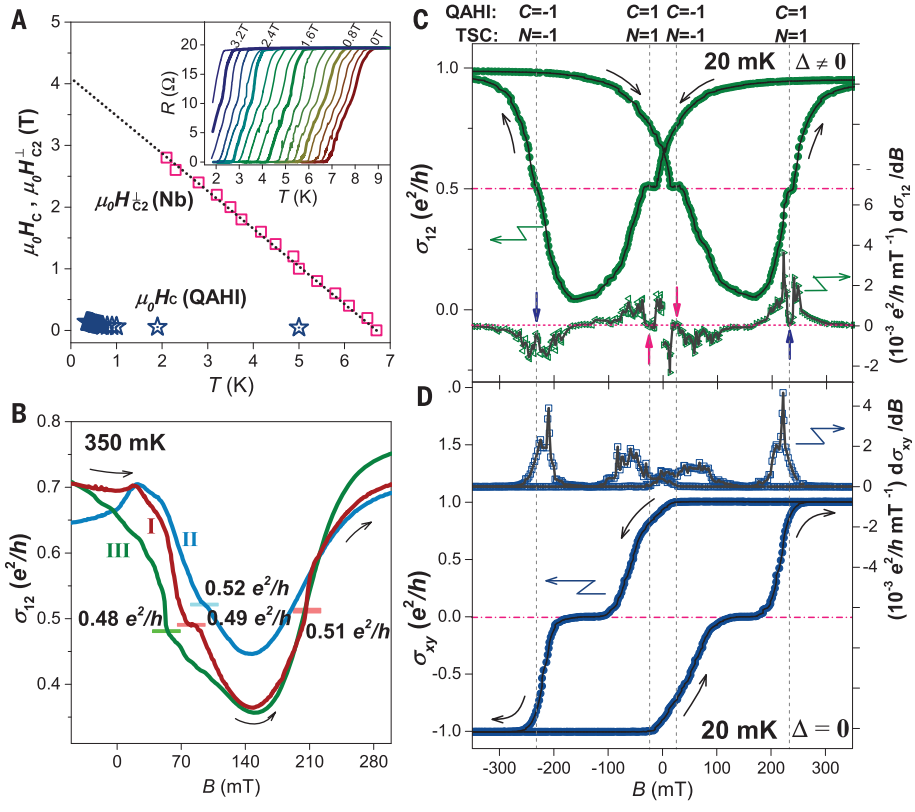

Fig. 2. Half-integer longitudinal conductance as a signature of single chiral Majorana edge modes. (**A**) Temperature-dependent perpendicular upper critical field ($\mu_0 H_{C2}^{\perp}$, pink) of the Nb bar and coercive field ($\mu_0 H_C$, cyan) of the QAHI, in which the former was derived from the temperature at which the zero resistance state is just reached under various perpendicular magnetic fields (inset, temperature-dependent resistance curves under magnetic field from zero to 3.4 T in 200-mT steps), whereas the latter was extracted from the magnetic field dependences of Hall resistance at different temperatures (fig. S1). Standard linearized Ginzburg-Landau theory for superconducting film was used for the fitting of $\mu_0 H_{C2}^{\perp}$ (dotted line). The large difference between $\mu_0 H_{C2}^{\perp}$ and $\mu_0 H_C$ ensures the superconducting proximity effect from Nb to QAHI. (**B**) The longitudinal four-terminal conductance (σ_{12}) of three representative TSC devices as functions of perpendicular magnetic fields at 350 mK. The three devices all show conductance plateaus at the low-field shoulders of the σ_{12} valleys with values close to the predicted 0.5 e^2/h, supporting the existence of single CMEM. Only Device I exhibits a sudden increase of σ_{12} at the high-field shoulder of the σ_{12} valley. (**C**) σ_{12} as a function of external perpendicular magnetic field obtained from Device I at 20 mK. When superconductivity is induced on the top surface of the QHAI, σ_{12} shows additional half-integer plateaus (~ 0.5 e^2/h) between the transitions of the QAHI$_{C=\pm1}$ and the normal insulator. (Lower plot) Derivative of σ_{12} with respect to the magnetic field. Topological transitions are marked by dashed lines and arrows. (**D**) Without superconducting proximity effect, the Hall conductance (σ_{xy}) of the QAHI device demonstrates the evolution between QAHI$_{C=\pm1}$ and the normal insulator, illustrating the surface-hybridization–induced zero plateaus at the coercive fields during magnetization reversals.

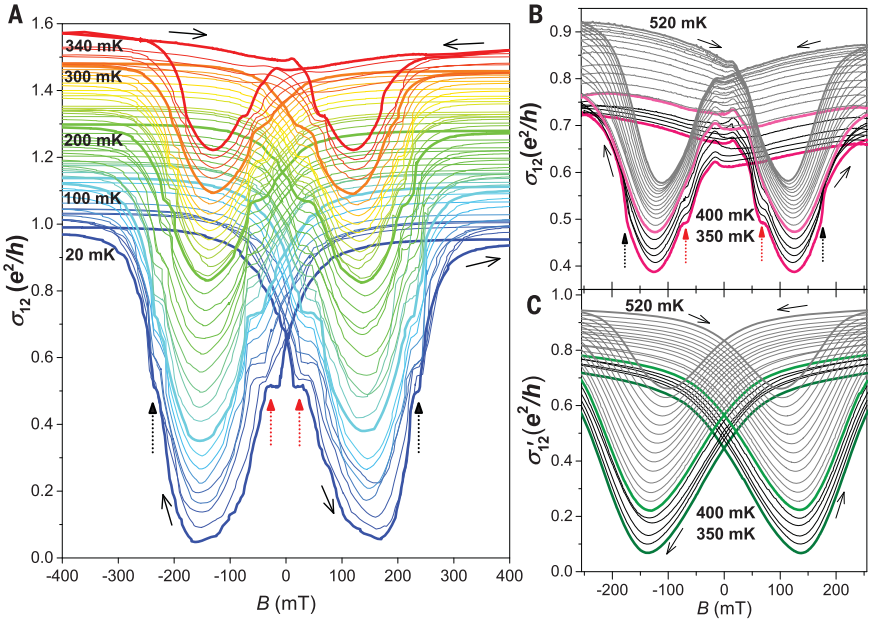

Fig. 3. Temperature evolution of the total longitudinal conductance in a TSC device. (**A** to **C**) Four-terminal magnetoconductance in [(A) and (B)] a TSC Device I (σ_{12}), and (C) a QAHI device (σ'_{12}), as functions of perpendicular magnetic fields at different temperatures. Traces are offset for clarity, except for the lowest traces at 20 mK in (A), 350 mK in (B), and 350 mK in (C), with 10-mK steps. To clearly demonstrate the temperature dependence, select traces are shown in bold, accompanied with corresponding temperatures. The half-integer plateaus gradually narrow down owing to the thermally activated bulk carriers and completely disappear above 400 mK for Device I as shown in (B) [compared with (C)]. Black and red dashed arrows indicate the half-plateau positions and solid black arrows denote field-scan directions.

similar magnetic field. These plateaus are close to the predicted value (0.5 e^2/h) where the transport in the TSC region is dominated by the 1D channel of the CMEM in the $\mathcal{N}$ = ±1 phase [see Fig. 1A, (ii) and (vi)]. Despite the fact that Majorana fermions are charge neutral, the two CMEMs at the two edges of the $TSC_{\mathcal{N}=\pm1}$ constitute a coherent charged basis that transmits exactly one-half of the incoming charges. At 20 mK, distinct plateaus with the quantized value of 0.50(±0.06) e^2/h are seen at both shoulders of the σ_{12} valleys (Fig. 2C). Outside the half-plateau regimes, when the magnetization is fully saturated, the conductance reaches a quantized value of 0.98(±0.04) e^2/h, indicating the $\mathcal{C}$ = ±1 / $\mathcal{N}$ = ±2 phases [see Fig. 1A, (i) and (vii)]. On the other hand, during the reversal of the magnetization, σ_{12} dips into a valley corresponding to the NI phase of the QAHI regions [see Fig. 1A, (iii), (iv), and (v)]. Ideally, the NI phase should completely shut down the QAHI channels, leading to zero-conductance plateaus. However, this requires an ultra-smooth sample such that the electrostatic fluctuations throughout the device are smaller than the hybridization gap (~4 meV) induced by the coupling between the top and bottom surface states of the QAHI thin film. Thanks to the proximity effect, band-bending may occur at the Nb covered region, such that the device may not be fully insulating as expected, resulting in a vanishingly small but observable residual σ_{12} of ~0.05 e^2/h observed in the NI phase (Fig. 2C). Furthermore, in this field range, the resistance between leads 1 and 2 can increase to as high as 10 to 100 MΩ (or even higher), which is comparable to the internal resistance of the lock-in amplifier instrument, making the accurate measurement of σ_{12} very challenging. Consistent with the phase transitions during the magnetic reversal, the half-integer plateaus (or kinks) occur at every reversal of the magnetization in the hysteresis loop. Such magnetization reversals can also be seen in a QAHI device with its Hall conductance (σ_{xy}) plotted in Fig. 2D aligned to Fig. 2C, where two intermediate zero plateaus (σ_{xy} ~ 0) induced by the NI-QAHI transition occur at the coercive fields H_C = ~±170 mT (*38*, *40*). In these half-integer plateaus (Fig. 2C), the transport in the TSC region is, in principle, purely dominated by a collection of chiral Majorana fermions as 1D edge modes. This feature is distinct from the "zero-bias conductance anomalies" induced by 0D Majorana bound states (*20*, *22*, *27*, *32*), and is as a hallmark signature associated with the chiral Majorana edge transport channels in the $TSC_{\mathcal{N}=\pm1}$ phases.

To further confirm the transport signature of the CMEMs in the $\mathcal{N}$ = ±1 phase, we carried out measurements at higher temperatures (Fig. 3A). With increasing temperature, the thermal broadening of the transport window gradually smeared the half-integer plateaus, which became kinks of finite slopes and then eventually disappeared above 400, 470, and 390 mK for Devices I (Fig. 3B), II (fig. S2A), and III (fig. S2B), respectively. In all three devices, the kinks at high-field reversals are always narrower than the low-field plateaus, and they vanish earlier as the temperature increases. This discrepancy between low-field and high-field reversals may be attributed to the magnetic field hindering the superconducting phase. Although the external magnetic field is lower than the critical field of the Nb bar (as shown in Fig. 2A), the interfacial exchange coupling between the Nb and the QAHI may provide a much larger effective field, which suppresses the superconducting phase in the TSC region.

Other effects that might lead to the observed transport signatures, such as the Barkhausen effect (*41*), must be ruled out. When domains are small and not strongly pinned by impurities, domain walls abruptly jump during the magnetization reversal, and the resultant stochastic Barkhausen steps therefore often appear in bunches that are irreproducible during different magnetic field sweeps. These steps mainly occur at small magnetic fields (fig. S3), and none of them could reach R_{xx} = 2 h/e^2 (supplementary text). In contrast, the CMEM-induced half-integer plateaus in Device I can be reproduced (fig. S4) with clear temperature traces (Fig. 3A), and they occur both in low-field and high-field cases (Fig. 2C). When large domains are pinned by impurities or defects, some Barkhausen steps can be retraceable at large magnetic fields, as shown in fig. S2A for Device II. However, these steps can be strongly suppressed with improved sample quality, as shown in Fig. 3A for Device I and fig. S2B for Device III. Among all three devices, only the 0.5 e^2/h plateaus survive in all cases, suggesting that they originate from a fundamentally different mechanism. Only the backscattering originating in the $TSC_{\mathcal{N}=\pm1}$ phase could lead to such a half-quantized conductance that persists in different batches of devices. Any backscattering processes from the $TSC_{\mathcal{N}=\pm2}$ or the $NSC_{\mathcal{N}=0}$ phase would have a considerably smaller Andreev scattering, which cannot explain the half-integer conductance.

Another alternative explanation of the half-integer σ_{12} might be that the two QAHI regions

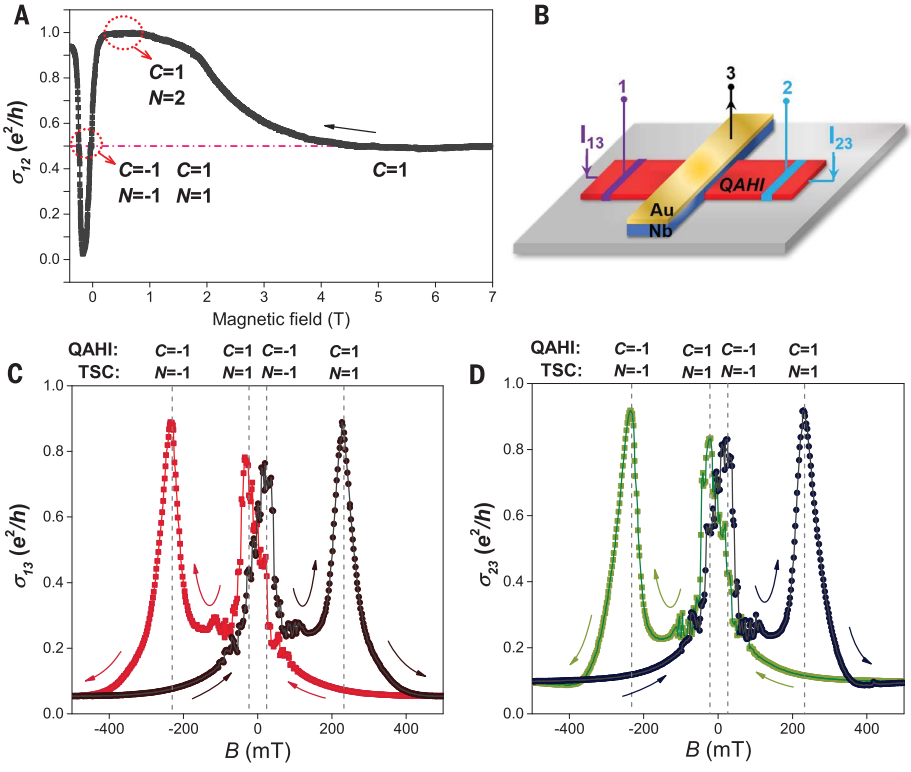

Fig. 4. Longitudinal conductance response to a high magnetic field and the conductance matrix in a TSC device. Shown are the data from Device I at 20 mK. (**A**) σ_{12} as a function of high external perpendicular magnetic field. At the upper critical field of the Nb bar of about 4 T at 20 mK (Fig. 2A), the superconductivity of Nb and the topological superconductivity underneath are expected to be eliminated. Afterward, the Nb bar becomes a floating metal and connects its left and right QAHI bars in series. Thus, σ_{12} gradually decreases as the field increases and quantizes to ~0.5 e^2/h when the field reaches about 4 T. (**B**) Schematic configuration of a TSC device for the conductance measurements. The three-terminal conductance (σ_{13} and σ_{23}) was obtained by passing a current from either the QAHI lead to the superconductor Nb (I_{13} and I_{23}) and measuring the corresponding potential drop (across points 1-3 and 2-3). (**C** and **D**) The resulting σ_{13} and σ_{23} as functions of external magnetic fields, respectively. The dashed lines align with those in Fig. 2, C and D; the arrows indicate magnetic field sweeping directions. During the transitions to a TSC ($\mathcal{N}$ = ±1), both σ_{13} and σ_{23} become close to e^2/h but almost vanish otherwise, consistent with the theoretical prediction of the single CMEMs.

could have been connected in series by a nonsuperconducting, topologically trivial Nb covered region. To address this issue, two additional transport measurements were carried out using Device I, as explained below.

First, σ_{12} was obtained at high magnetic fields as shown in Fig. 4A, using the same setup as Fig. 1B. After the magnetic field eliminates the superconducting phase in both layers, σ_{12} indeed reaches ~0.5 e^2/h, suggesting the scenario of two QAHIs connected in series as expected. This occurs when the external field exceeds ~4 T, the anticipated upper critical field of the Nb layer shown in Fig. 2A. This behavior suggests that the Nb covered region was indeed in a $TSC_{\mathcal{N}=2}$ phase before σ_{12} starting to drop back to ~0.5 e^2/h. If the half-integer plateaus below the critical field were induced by this trivial picture, they would have persisted all the way throughout large fields (fig. S5E). The coexistence of these 0.5 and 1.0 e^2/h plateaus in Fig. 4A rules out this trivial picture, providing again strong evidence that the low-field half-integer plateaus (within ±300 mT) have an origin different from that of the high-field one (4 to 7 T) and are likely associated with CMEMs.

Second, σ_{13} and σ_{23} were measured between electrodes 1-3 and 2-3 at 20 mK, respectively, using the setup shown in Fig. 4B. If the TSC were a trivial normal metal, the system should be equivalent to a QAHI that is directly contacted with two electrodes. Thus, a typical σ_{xx} behavior of a QAHI (Fig. 3C) should be observed—i.e., both σ_{13} and σ_{23} would exhibit two valleys at ±150 mT ($\mathcal{C}$ = 0) and then reach e^2/h after the magnetization saturates ($\mathcal{C}$ = ±1)—as shown in fig. S5F. However, the measurements (Figs. 4, C and D) show four peaks, instead of two valleys, in both σ_{13} and σ_{23}, coinciding with the half-integer plateaus given by the measurements of σ_{12}. The height of these peaks reaches ~0.9 e^2/h, very close to the quantized value expected from the Andreev reflection of a single CMEM ($\mathcal{N}$ = ±1) (*36*) (for an elaborated theoretical explanation using the Laudauer-Büttiker transport picture, see the supplementary text). This result also demonstrates that superconductivity in the QAHI layer was indeed induced owing to the proximity effect; otherwise, the observed peaks would not occur, and the conductance would remain small throughout the magnetic field scan.

The QAHI-superconductor system was realized as a prototype of the chiral TSC in two dimensions; more complex layouts could be engineered to host the bound states of Majorana fermions in solid state and enable their manipulation. The Majorana fermion modes are predicted to be topologically protected and thus may become a building block for robust topological quantum computing.

REFERENCES AND NOTES

1. E. Majorana, *Nuovo Cim.* **14**, 171–184 (1937).
2. A. Stern, *Nature* **464**, 187–193 (2010).
3. N. Read, D. Green, *Phys. Rev. B* **61**, 10267–10297 (2000).
4. A. Kitaev, *Ann. Phys.* **321**, 2–111 (2006).
5. J. D. Sau, R. M. Lutchyn, S. Tewari, S. Das Sarma, *Phys. Rev. Lett.* **104**, 040502 (2010).
6. J. Alicea, *Phys. Rev. B* **81**, 125318 (2010).
7. S. Nadj-Perge, I. K. Drozdov, B. A. Bernevig, A. Yazdani, *Phys. Rev. B* **88**, 020407 (2013).
8. B. Braunecker, P. Simon, *Phys. Rev. Lett.* **111**, 147202 (2013).
9. G. E. Volovik, *Sov. Phys. JETP* **69**, 9 (1988).
10. A. P. Schnyder, S. Ryu, A. Furusaki, A. W. W. Ludwig, *Phys. Rev. B* **78**, 195125 (2008).
11. X. L. Qi, T. L. Hughes, S. Raghu, S. C. Zhang, *Phys. Rev. Lett.* **102**, 187001 (2009).
12. A. Y. Kitaev, *Ann. Phys.* **303**, 2–30 (2003).
13. B. I. Halperin *et al.*, *Phys. Rev. B* **85**, 144501 (2012).
14. S. D. Sarma, M. Freedman, C. Nayak, *npj Quantum Information* **1**, 15001 (2015).
15. S. R. Elliott, M. Franz, *Rev. Mod. Phys.* **87**, 137–163 (2015).
16. X.-L. Qi, T. L. Hughes, S.-C. Zhang, *Phys. Rev. B* **82**, 184516 (2010).
17. S. B. Chung, X.-L. Qi, J. Maciejko, S.-C. Zhang, *Phys. Rev. B* **83**, 100512 (2011).
18. J. Wang, Q. Zhou, B. Lian, S.-C. Zhang, *Phys. Rev. B* **92**, 064520 (2015).
19. X.-L. Qi, S.-C. Zhang, *Rev. Mod. Phys.* **83**, 1057–1110 (2011).
20. V. Mourik *et al.*, *Science* **336**, 1003–1007 (2012).
21. S. Nadj-Perge *et al.*, *Science* **346**, 602–607 (2014).
22. A. Das *et al.*, *Nat. Phys.* **8**, 887–895 (2012).
23. A. R. Akhmerov, J. Nilsson, C. W. Beenakker, *Phys. Rev. Lett.* **102**, 216404 (2009).
24. K. T. Law, P. A. Lee, T. K. Ng, *Phys. Rev. Lett.* **103**, 237001 (2009).
25. J. Liu, A. C. Potter, K. T. Law, P. A. Lee, *Phys. Rev. Lett.* **109**, 267002 (2012).
26. J. J. He *et al.*, *Nat. Commun.* **5**, 3232 (2014).
27. J. P. Xu *et al.*, *Phys. Rev. Lett.* **114**, 017001 (2015).
28. M. X. Wang *et al.*, *Science* **336**, 52–55 (2012).
29. Y. Tanaka, T. Yokoyama, N. Nagaosa, *Phys. Rev. Lett.* **103**, 107002 (2009).
30. L. Fu, C. L. Kane, *Phys. Rev. Lett.* **100**, 096407 (2008).
31. L. Fu, C. L. Kane, *Phys. Rev. Lett.* **102**, 216403 (2009).
32. L. Maier *et al.*, *Phys. Rev. Lett.* **109**, 186806 (2012).
33. P. A. Lee, *Science* **346**, 545–546 (2014).
34. R. Žitko, J. S. Lim, R. López, R. Aguado, *Phys. Rev. B* **91**, 045441 (2015).
35. J. D. Sau, P. M. Brydon, *Phys. Rev. Lett.* **115**, 127003 (2015).
36. B. Lian, J. Wang, S.-C. Zhang, *Phys. Rev. B* **93**, 161401 (2016).
37. R. Yu *et al.*, *Science* **329**, 61–64 (2010).
38. X. Kou *et al.*, *Nat. Commun.* **6**, 8474 (2015).
39. Y. Feng *et al.*, *Phys. Rev. Lett.* **115**, 126801 (2015).
40. J. Wang, B. Lian, S.-C. Zhang, *Phys. Rev. B* **89**, 085106 (2014).
41. H. Barkhausen, *Phys. Z.* **20**, 401–403 (1919).

ACKNOWLEDGMENTS

This work was supported in part by the Spins and Heat in Nanoscale Electronic Systems (SHINES) Center, an Energy Frontier Research Center (EFRC) funded by the U.S. Department of Energy (DOE), Office of Science, Basic Energy Sciences under Award S000686. We are grateful for support from the Army Research Office (ARO) program under contract W911NF-15-1-0561:P00001 and NSF Faculty Early Career Development (CAREER) Award DMR-1350122. We also acknowledge support from the Function Accelerated nanoMaterial Engineering (FAME) Center, one of six centers of STARnet, a Semiconductor Research Corporation (SRC) program sponsored by Microelectronics Advanced Research Corporation (MARCO) and Defense Advanced Research Projects Agency (DARPA). Work at University of California, Davis, is supported by NSF ECCS-1232275 (K.L.), NSF DMR-1543582 (E.C.B), and NSF DMR-1610060 (Z.C.). J.W., B.L., Q.Z., and S.-C.Z. acknowledge support from the U.S. DOE, Office of Basic Energy Sciences, Division of Materials Sciences and Engineering, under contract DE-AC02-76SF00515 and from the NSF under grant DMR-1305677. A portion of this work was performed at the National High Magnetic Field Laboratory, which is supported by National Science Foundation Cooperative Agreement DMR-1157490 and the State of Florida. Q.L.H. thanks B. Shen for device fabrications. Z.C. and K.L. thank P. Klavins for technical assistance with superconductivity measurements. J.W. also acknowledges support from the National Thousand-Young-Talents Program.

SUPPLEMENTARY MATERIALS

www.sciencemag.org/content/357/6348/294/suppl/DC1
Materials and Methods
Supplementary Text
Figs. S1 to S6

2 June 2016; resubmitted 26 February 2017
Accepted 9 June 2017
10.1126/science.aag2792